Supporting Information

Dual-Redox-Sites Enable Two-Dimensional Conjugated Metal-Organic Frameworks with Large Pseudocapacitance and Wide Potential Window

Panpan Zhang,[1,‡] Mingchao Wang,[1,‡] Yannan Liu,[1] Sheng Yang,[1] Faxing Wang,[1] Yang Li,[2,3] Guangbo Chen,[1] Zichao Li,[4] Gang Wang,[1] Minshen Zhu,[2,3] Renhao Dong,[1,*] Minghao Yu,[1,*] Oliver G. Schmidt,[2,3] Xinliang Feng[1,*]

1. *Center for Advancing Electronics Dresden (cfaed) and Faculty of Chemistry and Food Chemistry, Technische Universität Dresden, Mommsenstr. 4, 01062 Dresden, Germany. E-mail: renhao.dong@tu-dresden.de; minghao.yu@tu-dresden.de; xinliang.feng@tu-dresden.de*

2. *Material Systems for Nanoelectronics, Chemnitz University of Technology, Reichenhainer Str. 70, 09107 Chemnitz, Germany.*

3. *Institute for Integrative Nanosciences, IFW Dresden, 01069 Dresden, Germany.*

4. *Helmholtz-Zentrum Dresden-Rossendorf, Institute of Ion Beam Physics and Materials Research, Bautzner Landstr. 400, 01328 Dresden, Germany.*

‡ *These authors contributed equally.*

Experimental methods

Materials. All the starting materials were purchased from commercial suppliers and used without further purification. Copper(II) phthalocyanine (99%, CuPc), 4,5-dichlorophthalonitrile (99%), $Cu(OAc)_2$ (98%), K_3PO_4 (98%), $Ni(NO_3)_2{\cdot}6H_2O$ (≥97.0%), $NiCl_2{\cdot}6H_2O$ (≥98%), $Cu(NO_3)_2{\cdot}3H_2O$ (99-104%), Na_2SO_4 (≥99.0%), and gelatin (tested according to Ph Eur) were purchased from Sigma-Aldrich Chemie GmbH. H_2SO_4 (≥95%), H_2O_2 (>30% w/v), and n-pentanol (99%) were provided by Fisher Scientific GmbH. 1,2,4,5-benzenetetramine tetrahydrochloride (97%), enzophenone imine (98%), *o*-phenylenediamine (99%), tris(dibenzylideneacetone) dipalladium(0) (99%), and racemic-2,2'-Bis(diphenylphosphino)-1,1'-binaphthyl (97%) were supplied by Fluorochem Limited. Ammonia solution (50% v/v) and 1,8-Diazabicyclo[5.4.0]undec-7-ene (99%) were obtained from abcr GmbH. The carbon cloth without a microporous layer (W0S1009, areal density: 12 mg cm^{-2}) was purchased from Fuel Cell Store, USA.

Pretreatment of carbon cloth. Carbon cloths were pretreated with piranha solution (H_2SO_4 : H_2O_2 = 7 : 3) at 60 °C overnight. Afterwards, they were washed with deionized water and acetone. Finally, the hydrophilic substrates were dried under vacuum overnight for further use.

In-situ growth of $M_2[CuPc(NH)_8]$ (M = Ni or Cu) on carbon cloth. Copper (II) 2,3,9,10,16,17,23,24-octaaminophthalocyanine octahydrochloride (OAPcCu, $CuPc(NH_2)_8{\cdot}8HCl$) was synthesized according to our previous report.[1] $CuPc(NH_2)_8{\cdot}8HCl$ (5 mg) was dissolved in dimethyl sulfoxide (DMSO, 3 mL) and ammonia solution (50% v/v, 0.1 mL) in a 10 mL vial. $Ni(NO_3)_2{\cdot}6H_2O$ (3 mg) in DMSO (1 mL) and ammonia solution (50% v/v, 0.1 mL) was added to the mixture in a sand bath at 60 °C under air. The reaction mixture was stirred for 10 min before it was transferred to a 10 mL vial with a piece of pretreated carbon cloth (1 cm × 3 cm, immersed part: 1 cm × 2 cm). After 8 h, the reaction mixture was cooled down to room temperature, and then the carbon cloth was taken out, washed with DMSO, H_2O, and acetone, respectively. Finally, it was dried under vacuum overnight, obtaining the

additive/binder-free electrode. The mass of $Ni_2[CuPc(NH)_8]$ grown on carbon cloth was measured by calculating the weight increase of the substrate after the *in-situ* growth with a microbalance (OHAUS Explorer® Analytical, the accuracy is 0.01 mg). The mass loading can be controlled from 0.5 to 2.0 mg cm^{-2} by repeated growth. If no otherwise specified, the areal loading mass of all the samples is about 1.1 mg cm^{-2}.

For the synthesis of $Cu_2[CuPc(NH)_8]$, $CuPc(NH_2)_8 \cdot 8HCl$ (5 mg) was dissolved in DMSO (3 mL) and ammonia solution (50% v/v, 0.1 mL) in a 10 mL vial with a piece of pretreated carbon cloth (1 cm × 3 cm, immersed part: 1 cm × 2 cm). $Cu(NO_3)_2 \cdot 3H_2O$ (2.5 mg) in DMSO (1 mL) and ammonia solution (50% v/v, 0.1 mL) was added to this mixture in a sand bath at 30 °C under air. The reaction mixture was stirred for 3 min and kept at this temperature for 8 h. The mass of $Cu_2[CuPc(NH)_8]$ grown on carbon cloth was measured by calculating the weight increase of the substrate after the *in-situ* growth with a microbalance (OHAUS Explorer® Analytical, the accuracy is 0.01 mg). The mass loading can be controlled from 0.5 to 2.0 mg cm^{-2} by repeated growth. If no otherwise specified, the areal loading mass of all the samples is about 1.1 mg cm^{-2}. The $M_2[CuPc(NH)_8]$ (M = Ni or Cu) powder samples were obtained without adding the carbon cloth by the same procedure.

Preparation of Ni(BTI) (BTI = 1,2,4,5-benzenetetraimine) coordination polymer on carbon cloth. A solution of $Ni(NO_3)_2 \cdot 6H_2O$ (11.9 mg) in water (2 mL) and ammonia solution (50% v/v, 0.3 mL) was added to a solution of 1,2,4,5-benzenetetramine tetrahydrochloride (14.2 mg) in water (7 mL) in a 15 mL vial with a piece of pretreated carbon cloth (1 cm × 3 cm, immersed part: 1 cm × 2 cm) at 60 °C in a sand bath. This mixture was stirred for 3 min and then kept for 2h. The obtained Ni(BTI) coordination polymer grown carbon cloth was washed for several times with deionized water and acetone, and finally dried under vacuum overnight. The areal loading mass is about 1.5 mg cm^{-2}.

Preparation of the CuPc electrode. The CuPc electrode was prepared by mixing commercial CuPc powder, acetylene black, and polytetrafluoroethylene (PTFE) in a weight ratio of 4:5:1

with the help of ethanol. The mixture was pressed into a film, and then dried at 80 °C overnight in a vacuum oven. After drying, the film was cut into many disks, which were subsequently pressed onto carbon cloths to act as the working electrodes. The areal loading mass is 1-2 mg cm^{-2}.

Preparation of the thick M_2[CuPc(NH)$_8$] (M = Ni or Cu) free-standing electrodes. The thick M_2[CuPc(NH)$_8$] free-standing electrodes were prepared by mixing M_2[CuPc(NH)$_8$] powders, acetylene black, and PTFE in a weight ratio of 7:2:1 with the help of ethanol. The mixture was pressed into a film, and then dried at 80 °C overnight in a vacuum oven. After drying, the film was cut into many disks with diameters of 8 mm. The areal loading mass is 10 mg cm^{-2}. The electrochemical measurements of the thick M_2[CuPc(NH)$_8$] electrodes were performed in the three-electrode Swagelok cell with the M_2[CuPc(NH)$_8$] disc as the working electrode, over-capacitive activated carbon as the counter electrode, a glass fiber separator (Whatman, GF/D) saturated with 1 M Na_2SO_4, and an Ag/AgCl (3 M KCl) reference electrode.

Fabrication of quasi-solid-state symmetric SCs. To fabricate quasi-solid-state symmetric SCs, two Ni_2[CuPc(NH)$_8$] electrodes were sandwiched together with a separator and gelatin/Na_2SO_4 gel electrolyte. The weight balance of the symmetric device was carried out based on equation ($C_+ \times \Delta E_+ \times m_+ = C_- \times \Delta E_- \times m_-$), where C is the specific capacitance in the three-electrode test, ΔE is the voltage range, and m is the mass of the active material. Based on the specific capacitances calculated from Figure S25, the mass ratio of the two Ni_2[CuPc(NH)$_8$] electrodes (m_+/m_-) is determined to be 1.4. The gelatin/Na_2SO_4 gel electrolyte was prepared by mixing gelatin powder (2 g) and Na_2SO_4 (2.84 g) in 20 mL deionized water at 65°C for 5 h with vigorously stirring until totally dissolved.

Density functional theory (DFT) calculations. A density functional mapping of Ni_2[CuPc(NH)$_8$] was carried out with the DFT method using Gaussian16 software package.[2] Structure of Ni_2[CuPc(NH)$_8$] were optimized with Becke's three-parameter hybrid exchange

functional and the Lee–Yang–Parr correlation functional (B3LYP) and the 6-311G (d,p) basis set. Surface charge mapping was visualized with GaussView 6.0 software.

Materials characterization. Scanning electron microscopy (SEM) and transmission electron microscopy (TEM) images were obtained with a field emission scanning electron microscope (FESEM, Zeiss Gemini 500) and a high-resolution transmission electron microscope (HRTEM, JEM-2100, JEOL, Japan), respectively. Raman analysis was performed by using a Raman microscope (LabRAM (HR 800), HORIBA JOBIN-Yvon) with a 532 nm Nd:YAG laser and a liquid-nitrogen cooled charge coupled device camera. The X-ray photoelectron spectroscopy (XPS) spectra were acquired using a Kratos Axis UltraDLD spectrometer (Kratos Analytical-A Shimadzu Group Company) with a monochromatic Al-Kα source (1486.6 eV). X-ray diffraction (XRD) patterns were obtained on an X-ray diffractometer (Dectris Mythen 1K Strip Detector, Stoe Stadi-P) using Cu-Kα radiation (λ = 0.154 nm) at 40 kV and 30 mA at room temperature. Electron paramagnetic resonance (EPR) spectra were collected on a Bruker BioSpin Gmbh spectrometer equipped with a standard mode cavity. Nitrogen adsorption isotherms were measured at 77.3 K with a Quantachrome SI-MP Instrument Automated Surface Area and Pore Size Analyzer.

Electrochemical measurement. Cyclic voltammetry (CV), galvanostatic charge/discharge (GCD) measurements, and electrochemical impedance spectroscopy (EIS) were employed with a CHI 660E electrochemical workstation. The electrochemical study of individual electrodes (1 cm × 2 cm) was performed in a three-electrode system with a Pt wire counter electrode and an Ag/AgCl (3 M KCl) reference electrode. For the linear sweep voltammetry (LSV) test of the aqueous electrolyte, two Pt foils and Ag/AgCl (3 M KCl) were employed as working, counter, and reference electrodes, respectively.

Calculations. The specific capacitance (C, F g^{-1}) based on the CV curves were calculated according to the following equation (1), where m is the mass of active material (g), v is the scan

rate (V s^{-1}), V_f and V_i are the integration potential limits of CV curves, $I(V)$ is the voltammetric current (in amperes), and $\int_{V_i}^{V_f} I(V)\,dV$ is the integrated area from CV curves.

$$C = \frac{1}{2 \times m \times v \times (V_f - V_i)} \int_{V_i}^{V_f} I(V)\,dV \quad (1)$$

The specific capacitance (C, F g^{-1}) was also calculated from the GCD curves according to the following equation (2), where I/m is the current density (A g^{-1}), t is the discharge time (s), and v is the voltage range (V).

$$C_A = \frac{I}{m} \times \frac{t}{v} \quad (2)$$

The areal energy densities (E, Wh kg^{-1}) and power densities (P, W kg^{-1}) were calculated from equations (3) and (4), where $\triangle V$ is the discharge voltage range (V) and $\triangle t$ is discharge time (s).

$$E = \frac{1}{2} \times C \times \frac{(\Delta V)^2}{3{,}600} \quad (3)$$

$$P = \frac{E}{\Delta t} \times 3600 \quad (4)$$

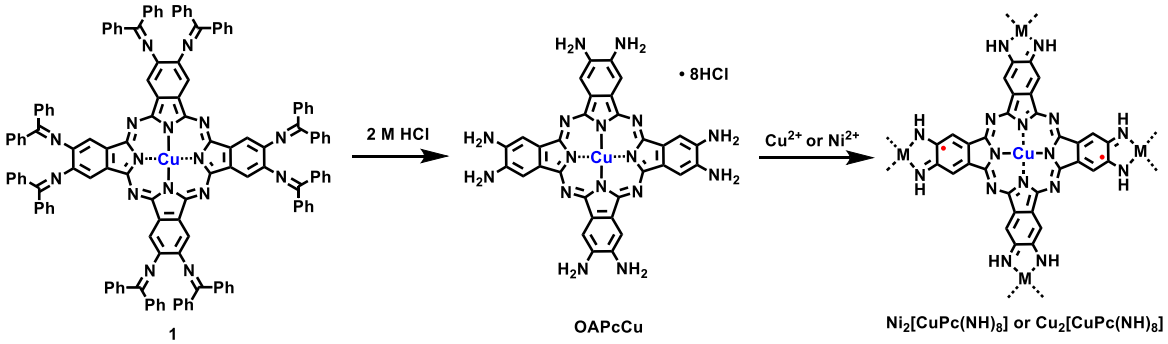

Figure S1. The synthetic route of $M_2[CuPc(NH)_8]$.

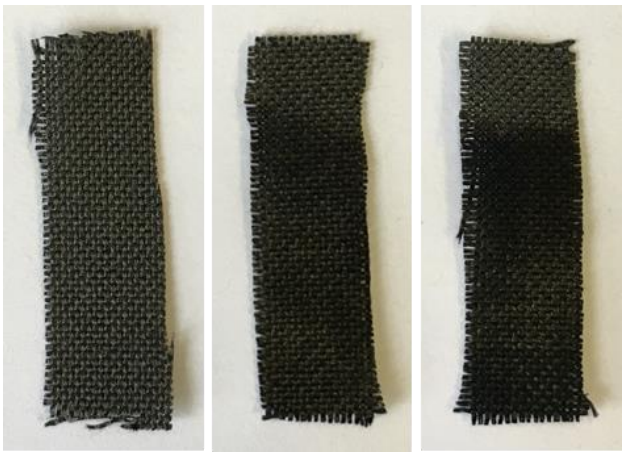

Figure S2. Digital photos of pristine carbon cloth (left), the $Ni_2[CuPc(NH)_8]$ electrode (middle), and the $Cu_2[CuPc(NH)_8]$ electrode (right).

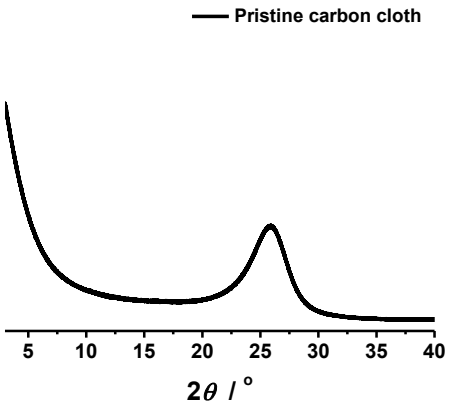

Figure S3. XRD pattern of the pristine carbon cloth.

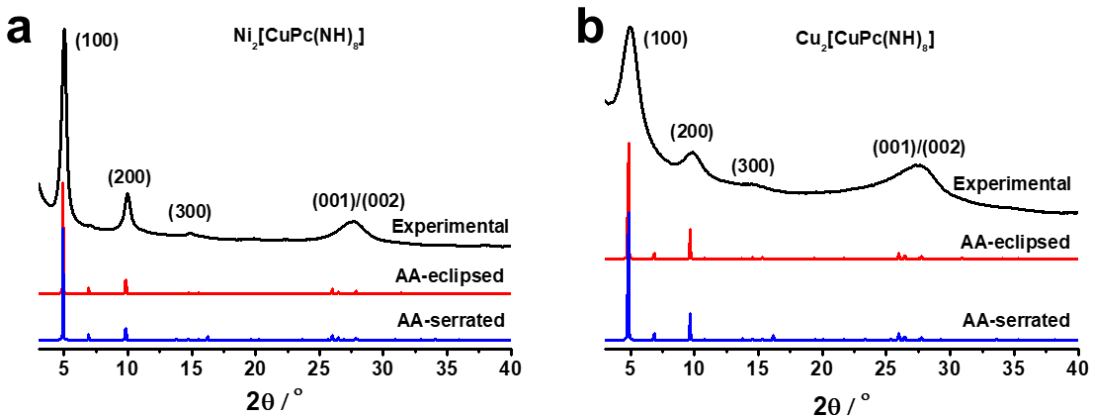

Figure S4. Experimental and simulated XRD patterns of (a) $Ni_2[CuPc(NH)_8]$ and (b) $Cu_2[CuPc(NH)_8]$.

Earlier studies verified the four-coordination geometries of the metal-bis(iminobenzosemiquinoid) model compounds ($M[C_6H_4(NH)_2]_2$, M = Ni or Cu), which serve as the linkage in our $M_2[CuPc(NH)_8]$ 2D *c*-MOF, *e.g.*, nickel-bis(iminobenzosemiquinoid) (*J. Am. Chem. Soc.* **1966**, *88*, 5201) and copper-bis(iminobenzosemiquinoid) (*Polyhedron* **1991**, *10*, 955). Moreover, in the previously reported M-NH-linked (M = Ni or Cu) 2D *c*-MOFs (based on benzene/triphenylene, *e.g.*, *J. Am. Chem. Soc.* **2014**, *136*, 8859; *Nat. Energy* **2018**, *3*, 30; *Angew. Chem. Int. Ed.* **2015**, *54*, 4349; *J. Am. Chem. Soc.* **2017**, *139*, 13608), both the Ni-NH and Cu-NH linkages were confirmed to possess a four-coordination geometry by identifying the consistency of experimental as well as calculated XRD patterns and comparing the peak positions in the experimental XRD patterns for Ni-NH- and Cu-NH-linked MOFs. Based on the literature information, the DFT calculation was employed in our study to simulate the structures of $M_2[CuPc(NH)_8]$ with the four-coordination geometry. We found that our experimental XRD results (Figure 1b) agree well with the simulated results (Figure S4-S6). Thereby, we conclude that both $Ni_2[CuPc(NH)_8]$ and $Cu_2[CuPc(NH)_8]$ are indeed equipped with four-coordination M-NH-linkage.

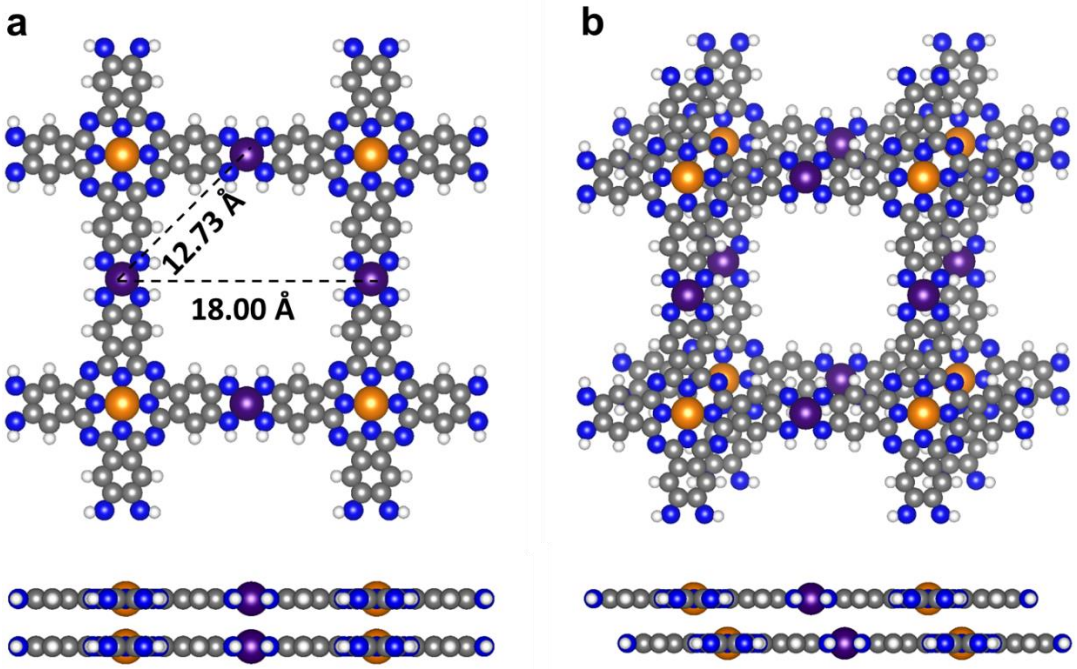

Figure S5. Top and side views of simulated (a) AA-eclipsed and (b) AA-serrated stacked bilayer of $Ni_2[CuPc(NH)_8]$ (C: grey, N: blue, Cu: orange, Ni: purple, H: white). $Ni_2[CuPc(NH)_8]$ can be defined by square unit cells with a=b=18.0 Å. The Ni-Ni distances are calculated as 12.73 and 18.00 Å in the 2D plane.

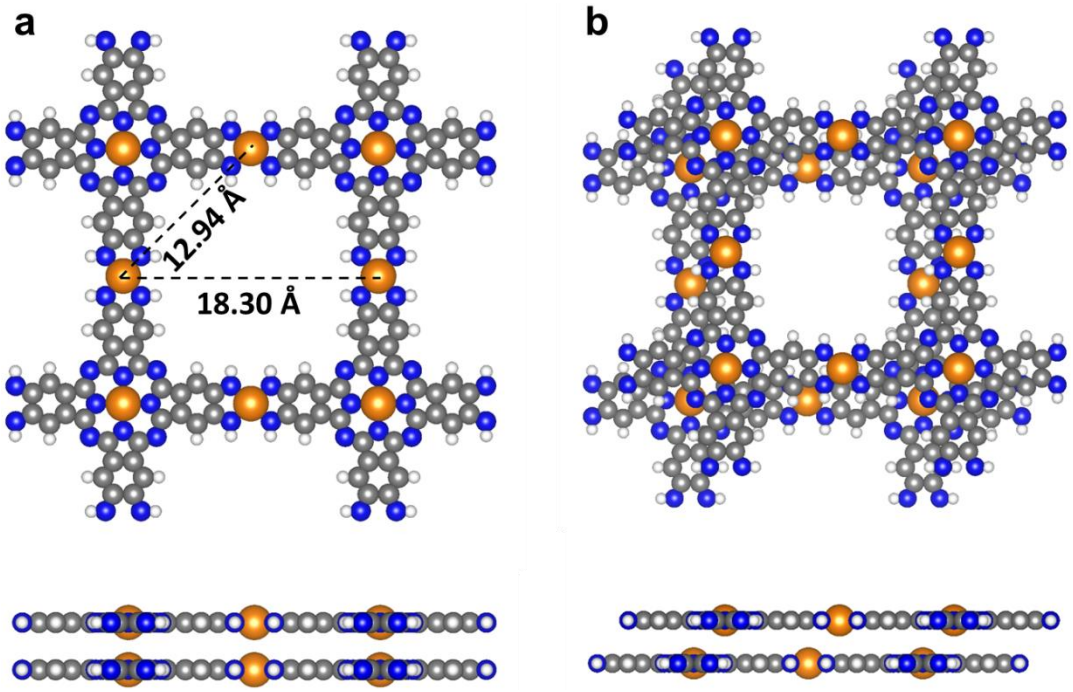

Figure S6. Top and side views of simulated (a) AA-eclipsed and (b) AA-serrated stacked bilayer of $Cu_2[CuPc(NH)_8]$ (C: grey, N: blue, Cu: orange, H: white). $Cu_2[CuPc(NH)_8]$ can be defined by square unit cells with a=b=18.30 Å. The Cu-Cu distances are calculated as 9.15, 12.94, and 18.30 Å in the 2D plane.

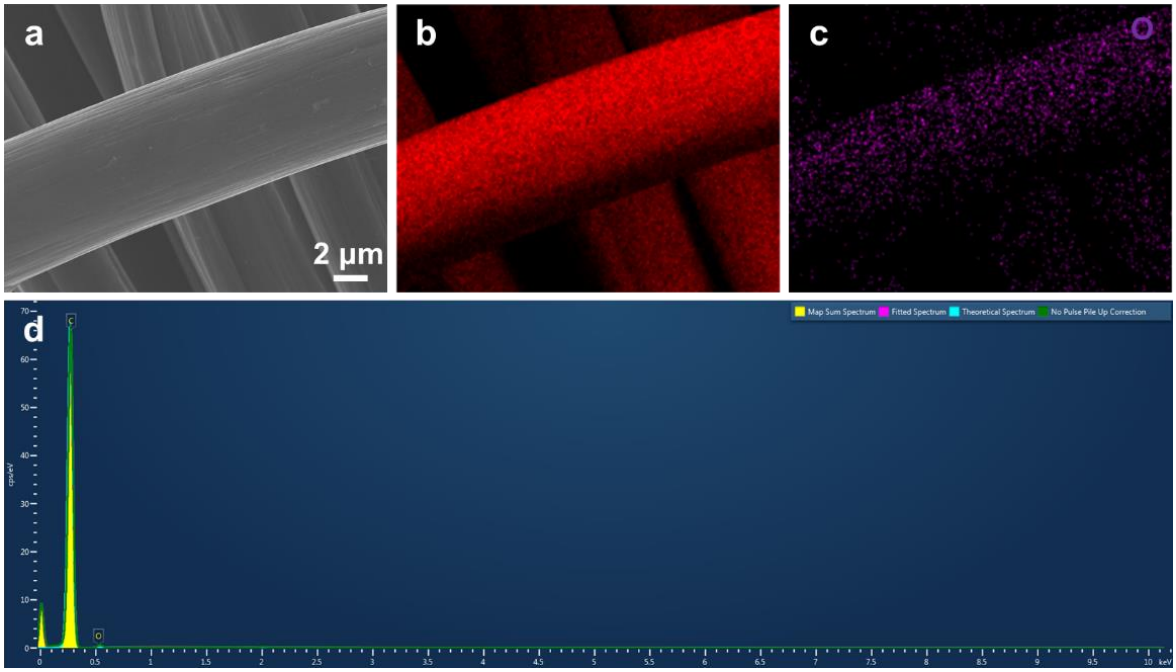

Figure S7. (a) SEM image of pristine carbon cloth. (b, c) Corresponding EDX elemental mapping analysis. (d) EDX spectrum of C and O elements.

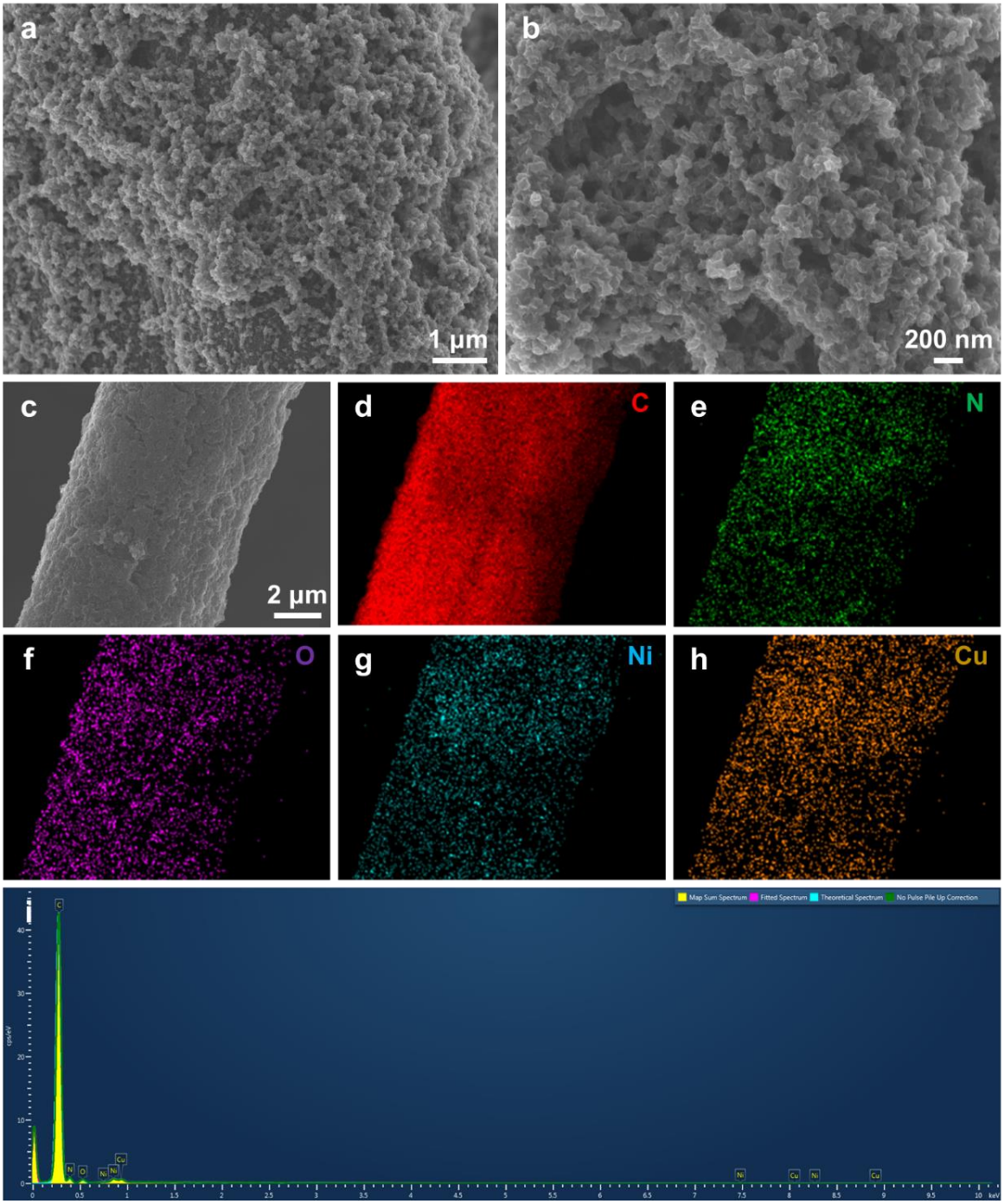

Figure S8. (a, b) SEM images of the $Ni_2[CuPc(NH)_8]$ electrode with different magnifications. (c-h) Corresponding EDX elemental mapping analysis. (i) EDX spectrum of C, N, O, Ni, Cu elements. The signal of O element is from carbon cloth or adsorbed moisture/O_2.

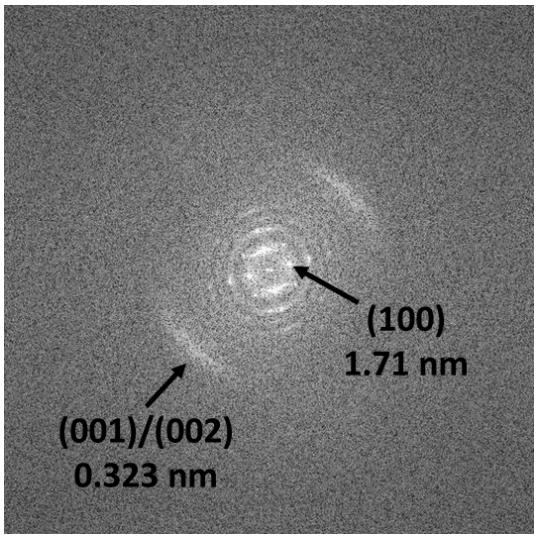

Figure S9. Fast Fourier transform pattern of $Ni_2[CuPc(NH)_8]$.

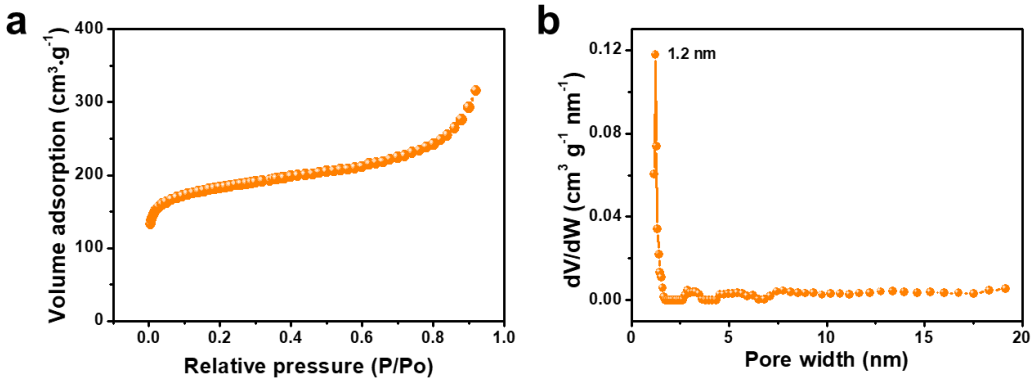

Figure S10. (a) Nitrogen adsorption isothermal curve and (b) pore-size distribution of $Ni_2[CuPc(NH)_8]$.

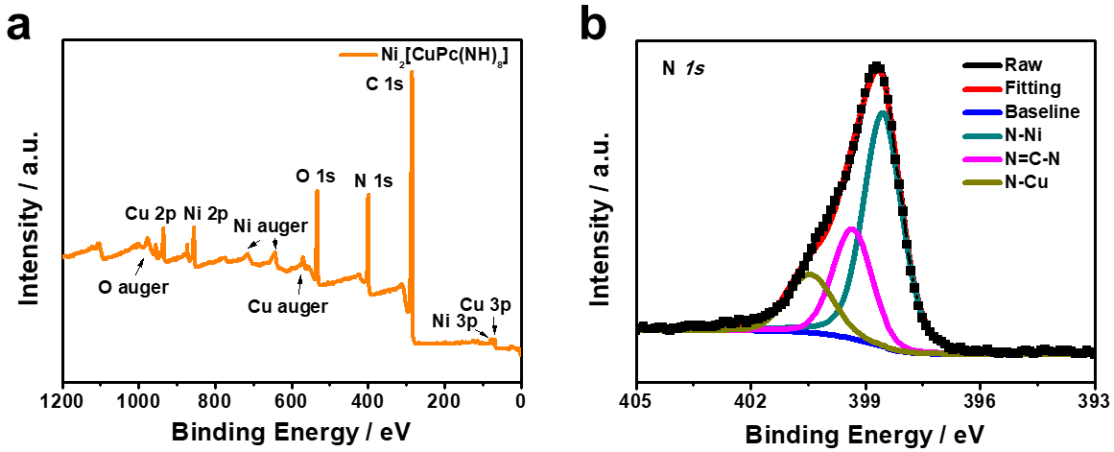

Figure S11. (a) XPS survey spectrum and (b) N 1*s* XPS spectrum of the $Ni_2[CuPc(NH)_8]$ electrode.

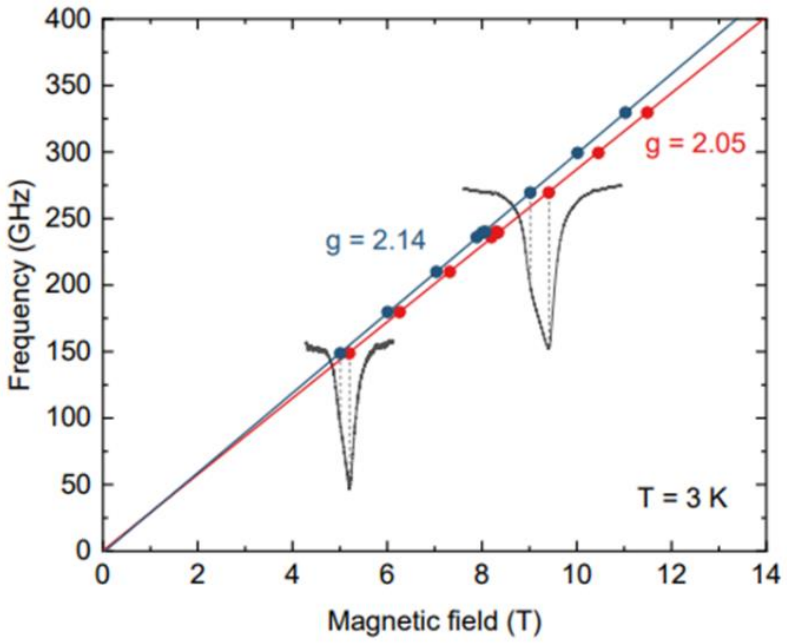

Figure S12. EPR spectrum of $Ni_2[CuPc(NH)_8]$ recorded at 3 K. EPR spectroscopy of $Ni_2[CuPc(NH)_8]$ presents a main peak with a *g*-factor of 2.05 and a shoulder with a *g*-factor of 2.14, which correspond to the Cu^{II} atoms in the CuPc unit. Furthermore, the EPR spectrum of $Ni_2[CuPc(NH)_8]$ displays no signals for organic radicals. The XPS spectra reveal the absence of charge-balancing counter ions and suggest a charge-neutral framework. Based on the XPS and EPR results, we propose a reasonable radical structure in Figure 1a, which remains conjugated and contains delocalized diradical in the CuPc unit.

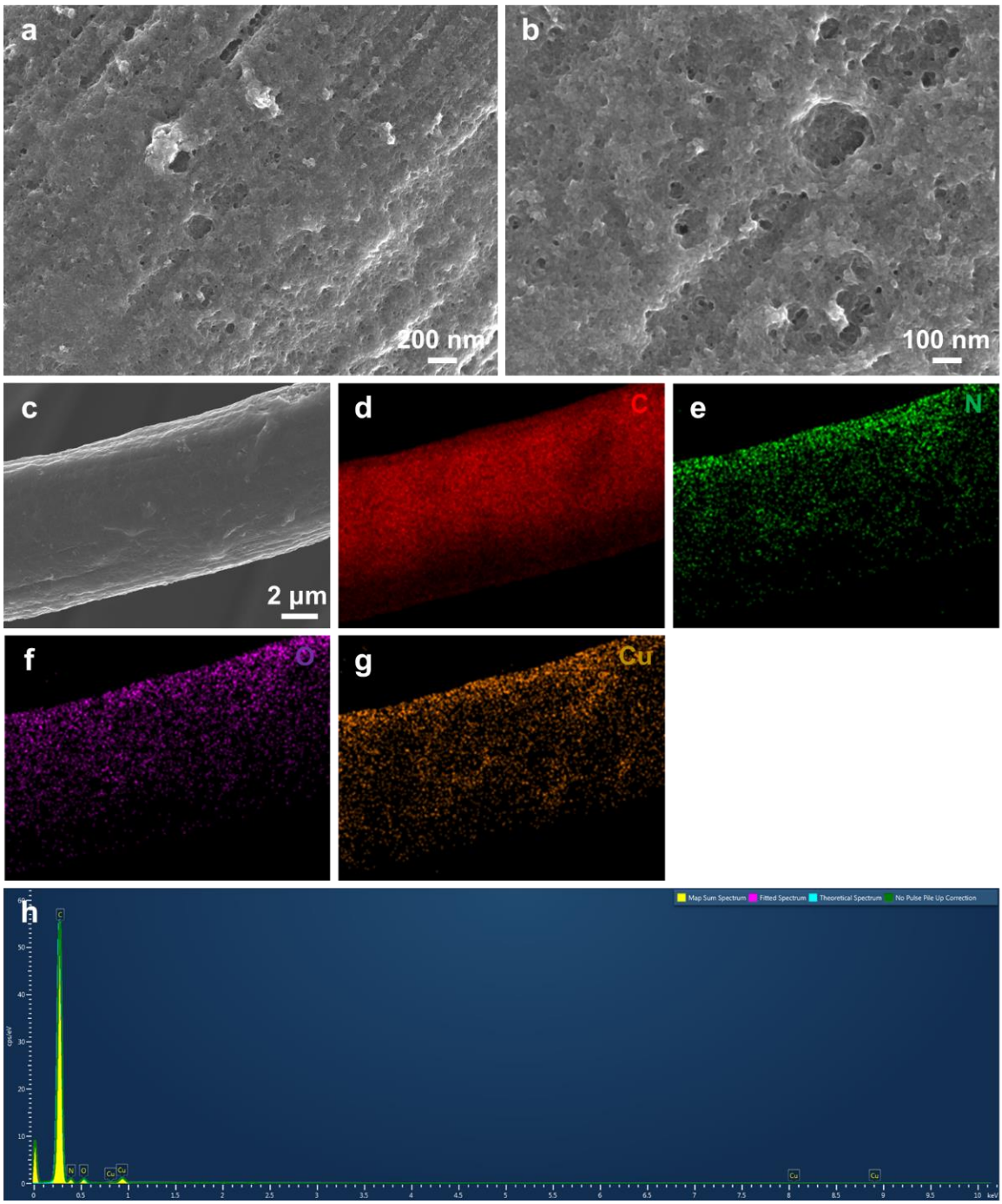

Figure S13. (a, b) SEM images of the $Cu_2[CuPc(NH)_8]$ electrode with different magnifications. (c-g) Corresponding energy-dispersive X-ray (EDX) elemental mapping analysis. (h) EDX spectrum of C, N, O, Cu elements. The signal of O element is from carbon cloth or adsorbed moisture/O_2.

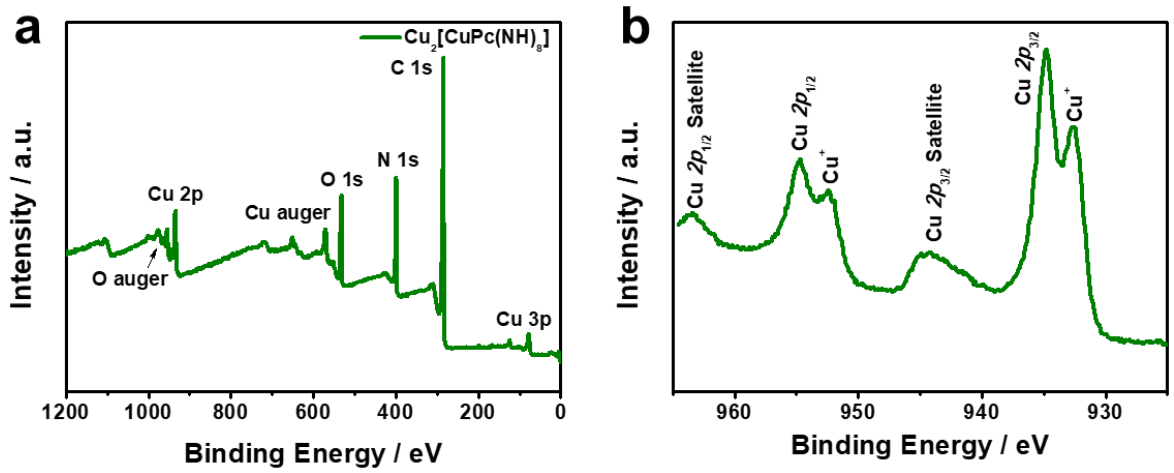

Figure S14. (a) XPS survey spectrum and (b) Cu 2*p* XPS spectrum of the $Cu_2[CuPc(NH)_8]$ electrode. $Cu_2[CuPc(NH)_8]$ displays splitting Cu $2p_{1/2}$ (954.7 and 952.4 eV) and Cu $2p_{3/2}$ peaks (934.9 and 932.6 eV), which are indicative of mixed-valence Cu atoms ($Cu^{I/II}$).[3-4]

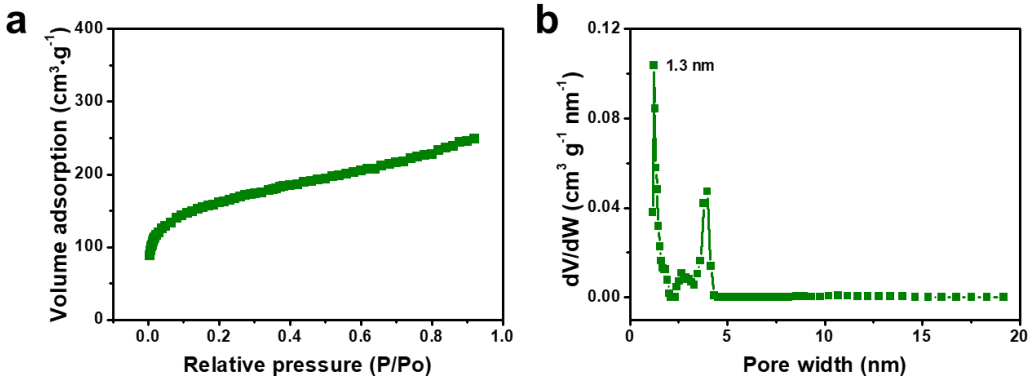

Figure S15. (a) Nitrogen adsorption isothermal curve and (b) pore-size distribution of $Cu_2[CuPc(NH)_8]$. The specific surface area of $Cu_2[CuPc(NH)_8]$ is 556 $m^2\ g^{-1}$, and the main size of the micropores is about 1.3 nm.

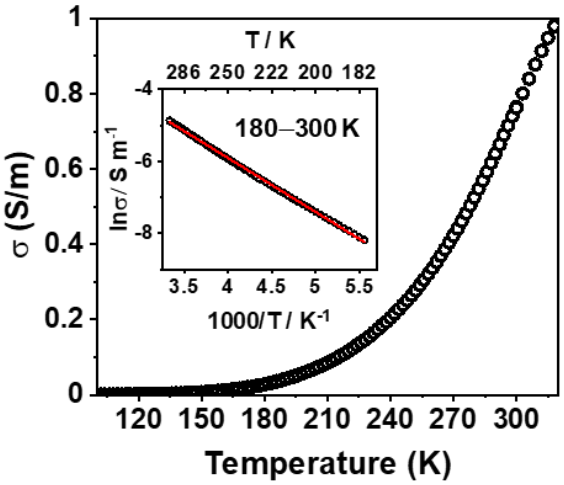

Figure S16. Variable-temperature electrical conductivity of $Ni_2[CuPc(NH)_8]$. The inset is lnσ as a function of 1000/T. The activation energy in the temperature region of 180–300 K was calculated as 0.13 eV.

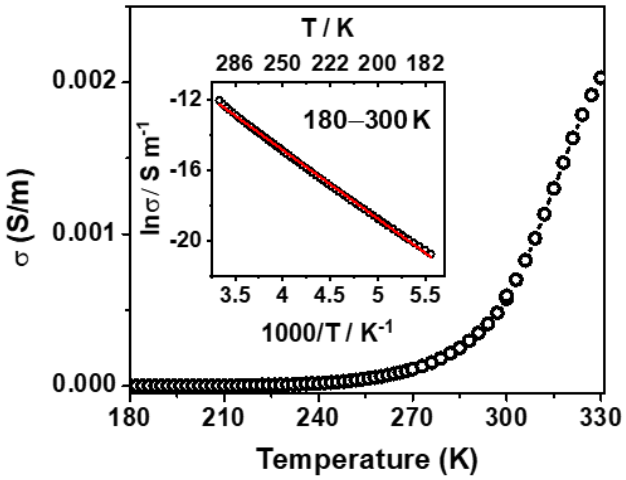

Figure S17. Variable-temperature electrical conductivity of $Cu_2[CuPc(NH)_8]$. The inset is lnσ as a function of 1000/T. The activation energy in the temperature region of 180–300 K was calculated as 0.34 eV.

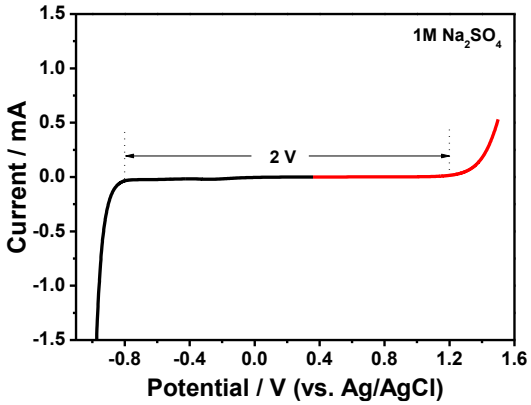

Figure S18. LSV curve with a scan rate of 1 mV s^{-1} for 1 M Na_2SO_4 aqueous electrolyte.

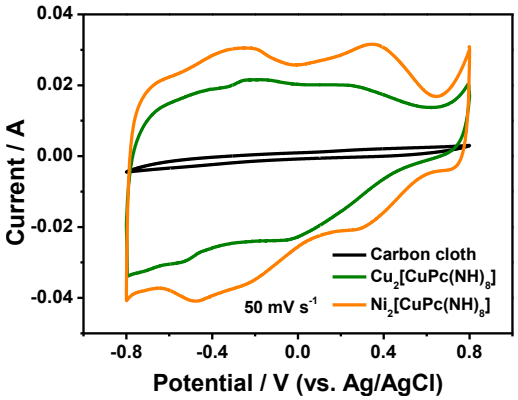

Figure S19. CV curves of pristine carbon cloth, the $Cu_2[CuPc(NH)_8]$ electrode, and the $Ni_2[CuPc(NH)_8]$ electrode at 50 mV s^{-1} in the three-electrode system.

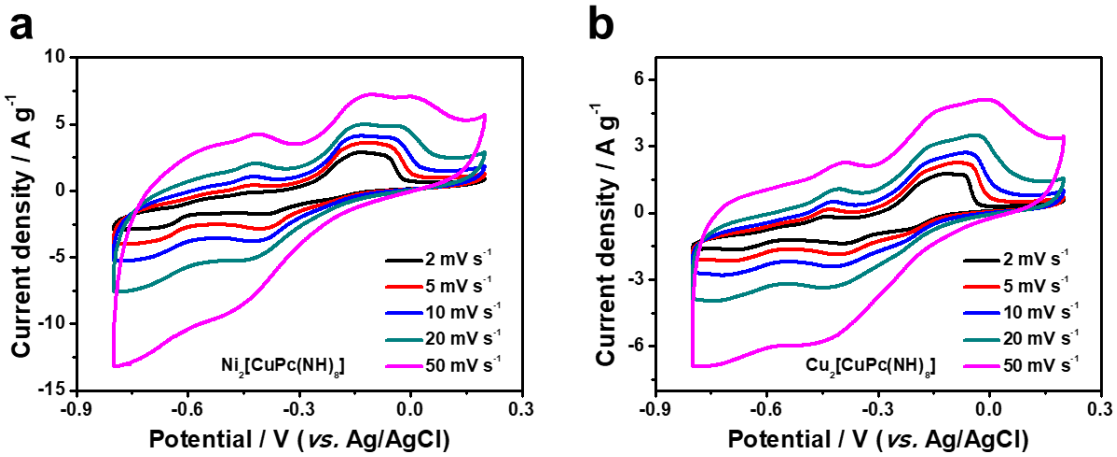

Figure S20. CV curves of (a) the $Ni_2[CuPc(NH)_8]$ electrode and (b) the $Cu_2[CuPc(NH)_8]$ electrode tested in 1 M KOH with the three-electrode system.

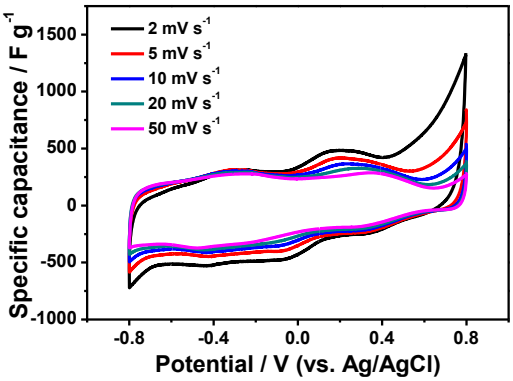

Figure S21. Normalized CV curves of the $Ni_2[CuPc(NH)_8]$ electrode at various scan rates.

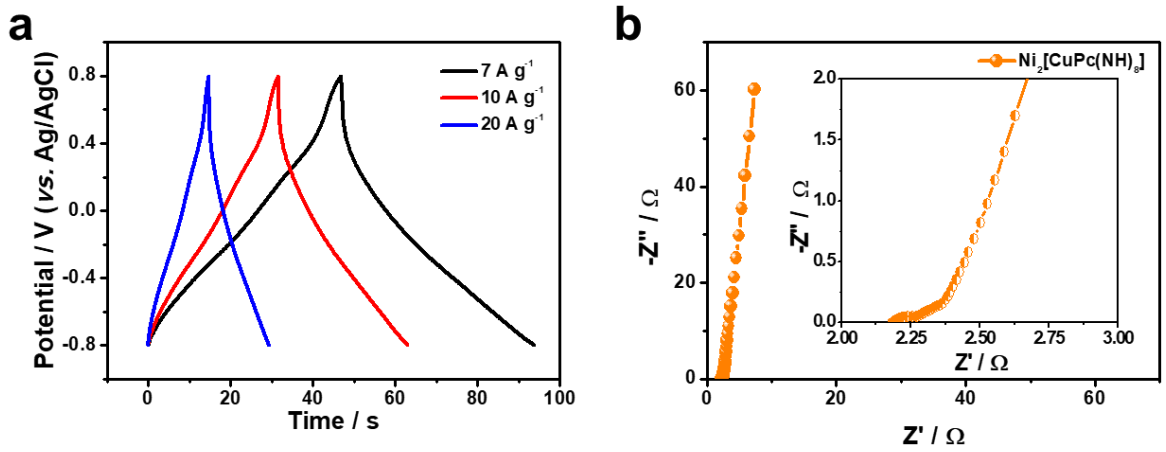

Figure S22. Electrochemical performance of the $Ni_2[CuPc(NH)_8]$ electrode in three-electrode system. (a) GCD curves from 7 to 20 A g^{-1}. (b) Nyquist plots before measurement. Inset depicts an enlarged high-frequency region.

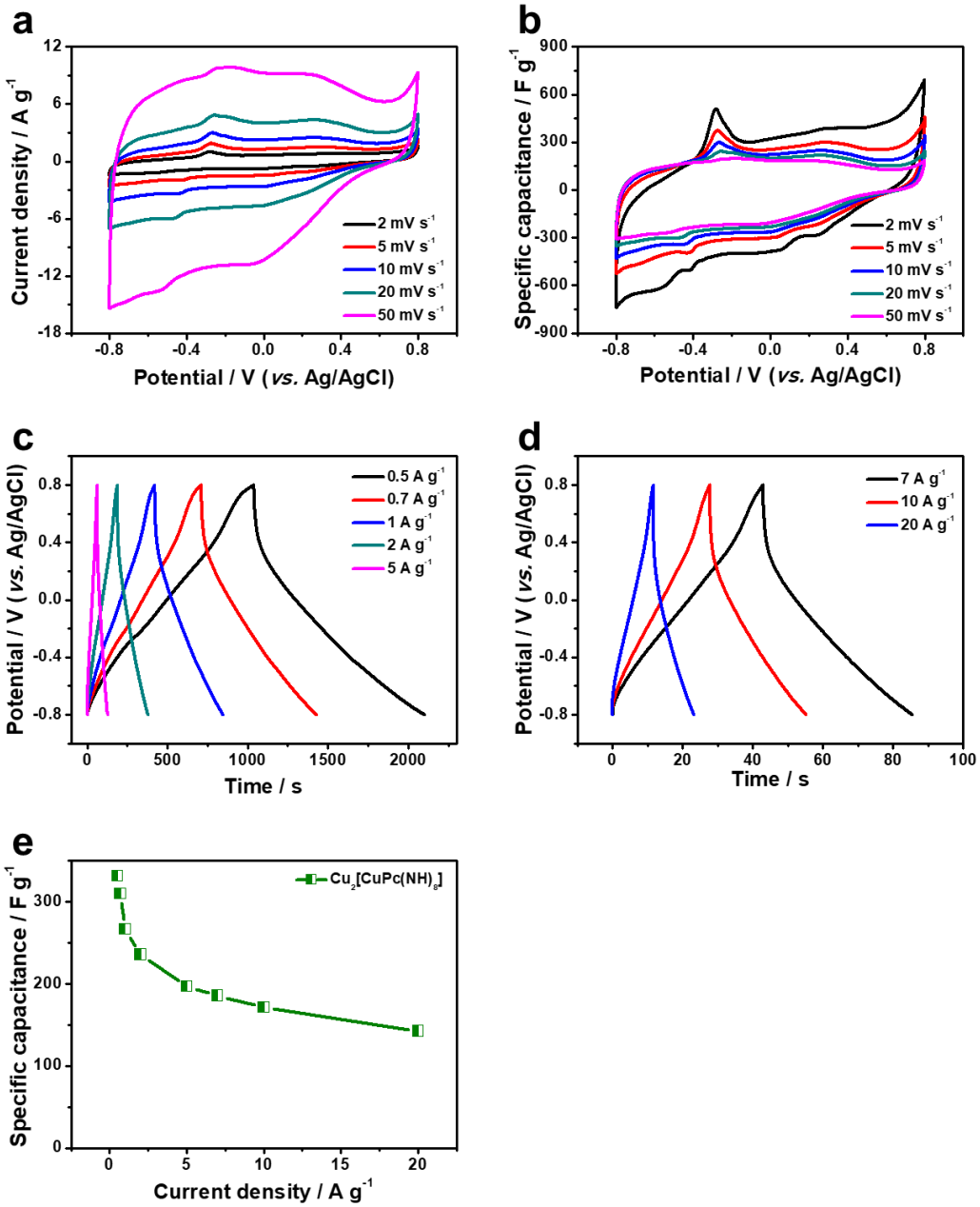

Figure S23. Electrochemical performance of the $Cu_2[CuPc(NH)_8]$ electrode in three-electrode system. (a, b) CV curves and normalized CV curves from 2 to 50 mV s^{-1}. (c, d) GCD curves from 0.5 to 20 A g^{-1}. (e) Specific capacitances calculated from GCD curves as a function of current density. The specific capacitance calculated from the GCD curves is 332 F g^{-1} at a current density of 0.5 A g^{-1}.

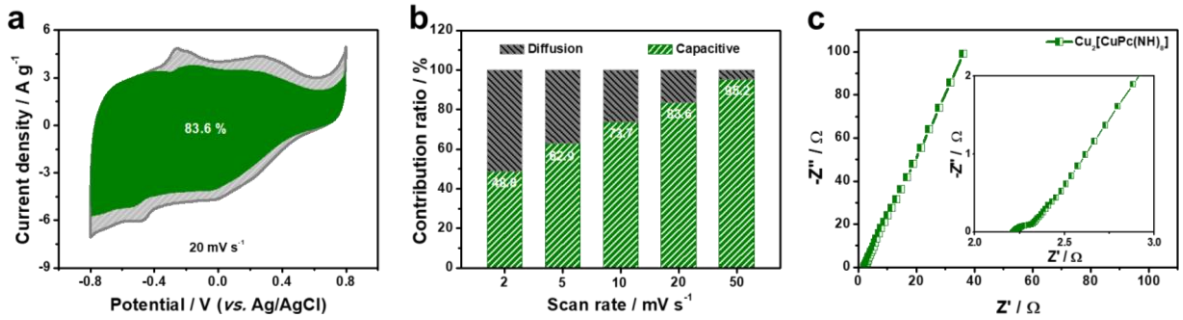

Figure S24. Electrochemical performance of the $Cu_2[CuPc(NH)_8]$ electrode in three-electrode system. (a) CV curve with separation between the total current and the capacitive (green) current at 20 mV s^{-1}. (b) Normalized contribution ratios of the capacitive (green) and diffusion-controlled (black) components as a function of scan rate. (c) Nyquist plots before measurement. Inset depicts an enlarged high-frequency region.

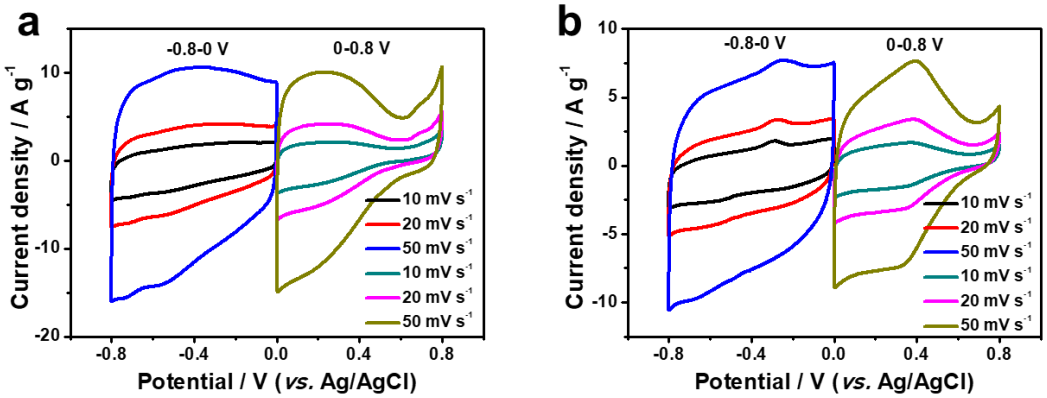

Figure S25. CV curves on both sides of open-circuit potentials (OCPs) at 10, 20, and 50 mV s^{-1} of (a) the $Ni_2[CuPc(NH)_8]$ electrode and (b) the $Cu_2[CuPc(NH)_8]$ electrode. The OCPs of $Ni_2[CuPc(NH)_8]$ and $Cu_2[CuPc(NH)_8]$ were measured to be 0.01 and −0.02 V, respectively. According to the CV curves, the specific capacitances of $Ni_2[CuPc(NH)_8]$ are 191.7 F g^{-1} (−0.8-0 V) and 141.2 F g^{-1} (0-0.8 V) at 10 mV s^{-1}, respectively. Meanwhile, the specific capacitances of $Cu_2[CuPc(NH)_8]$ are calculated to be 154.6 F g^{-1} (−0.8-0 V) and 111.4 F g^{-1} (0-0.8 V) at 10 mV s^{-1}, respectively. According to these calculated specific capacitances, we assembled the two-electrode quasi-solid-state supercapacitors based on the $Ni_2[CuPc(NH)_8]$ electrodes.

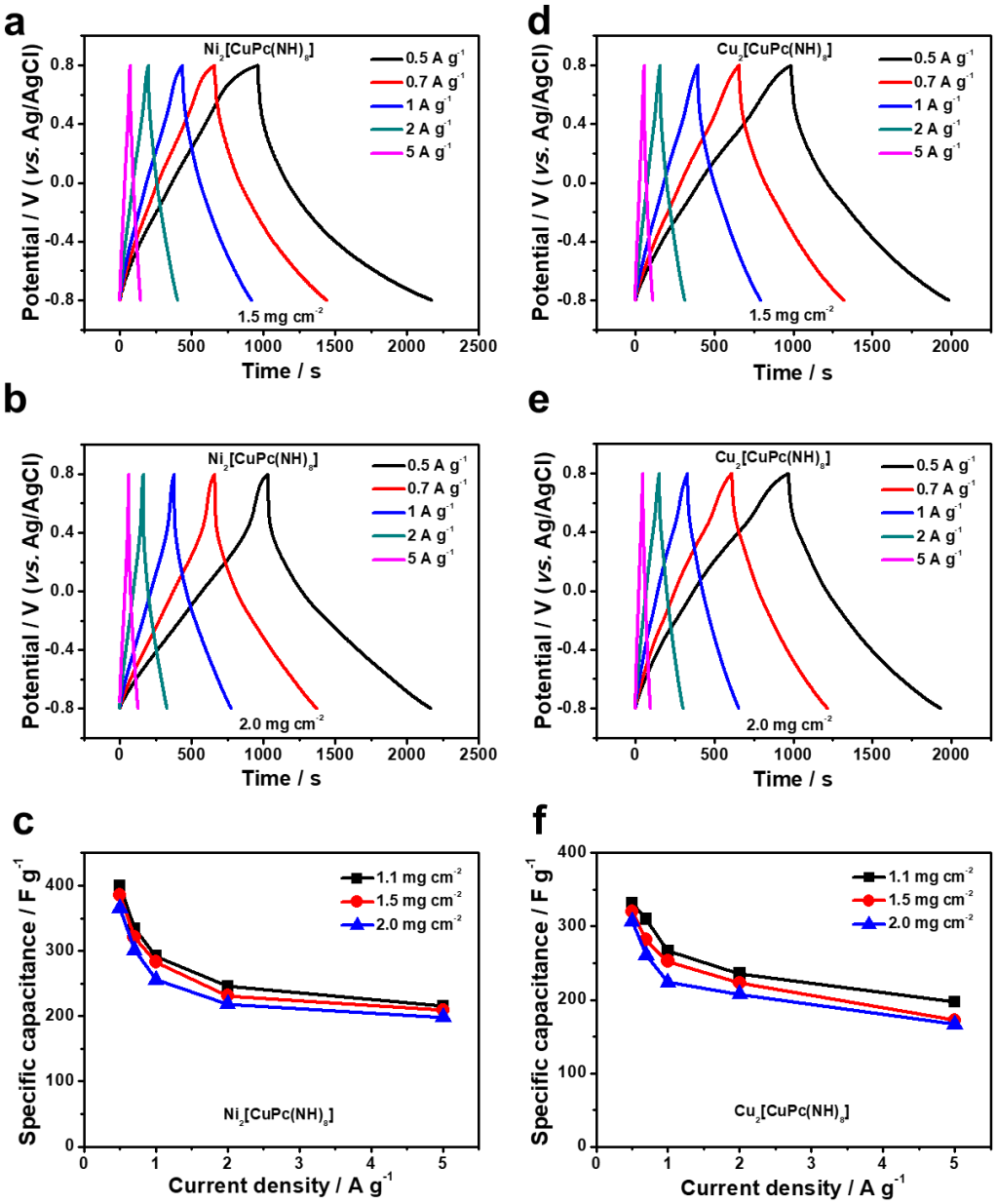

Figure S26. Specific capacitances of (a-c) the $Ni_2[CuPc(NH)_8]$ electrodes and (d-f) the $Cu_2[CuPc(NH)_8]$ electrodes with different mass loadings as a function of current densities. The maximum specific capacitances of $Ni_2[CuPc(NH)_8]$ electrodes with the mass loading of 1.1, 1.5, and 2.0 mg cm^{-2} are 399.7, 385.6, and 365.3 F g^{-1}, respectively. The maximum specific capacitances of $Cu_2[CuPc(NH)_8]$ electrodes with the mass loading of 1.1, 1.5, and 2.0 mg cm^{-2} are 331.9, 320.2, and 306.9 F g^{-1}, respectively.

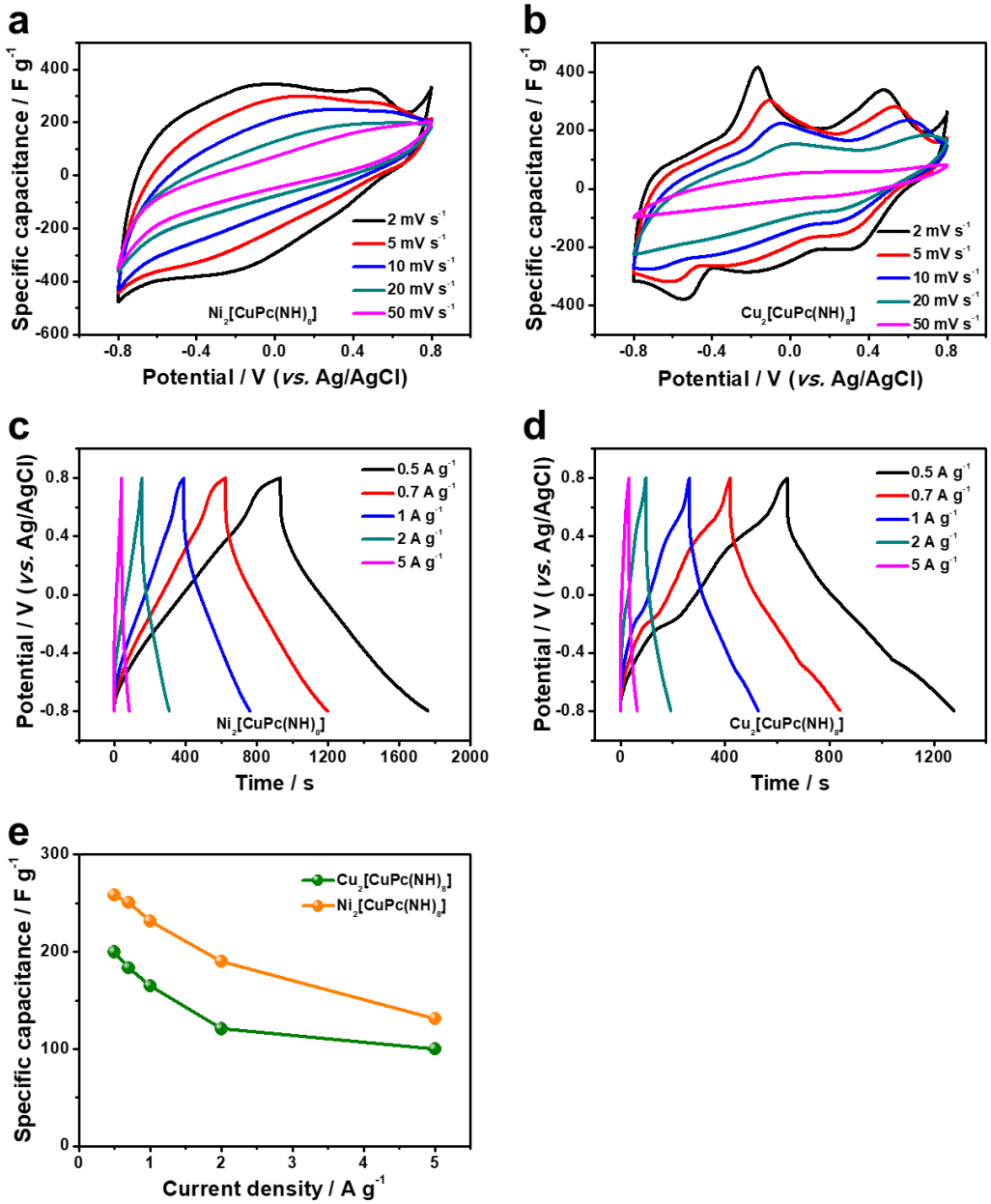

Figure S27. Electrochemical performance of the thick $M_2[CuPc(NH)_8]$ free-standing electrodes in the three-electrode Swagelok cell. (a, b) CV curves from 2 to 50 mV s^{-1}. (c, d) GCD curves from 0.5 to 5 A g^{-1}. (e) Specific capacitances calculated from GCD curves as a function of current density.

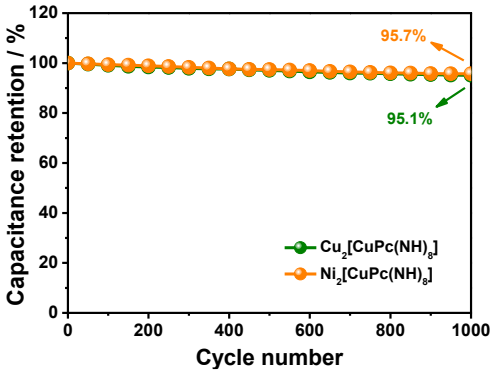

Figure S28. Cycling performance of the M_2[CuPc(NH)$_8$] electrodes at a current density of 1 A g^{-1}. After 1000 charge/discharge cycles at 1 A g^{-1}, the Ni_2[CuPc(NH)$_8$] and Cu_2[CuPc(NH)$_8$] electrodes are able to retain 95.7% and 95.1% of their initial capacitances, respectively.

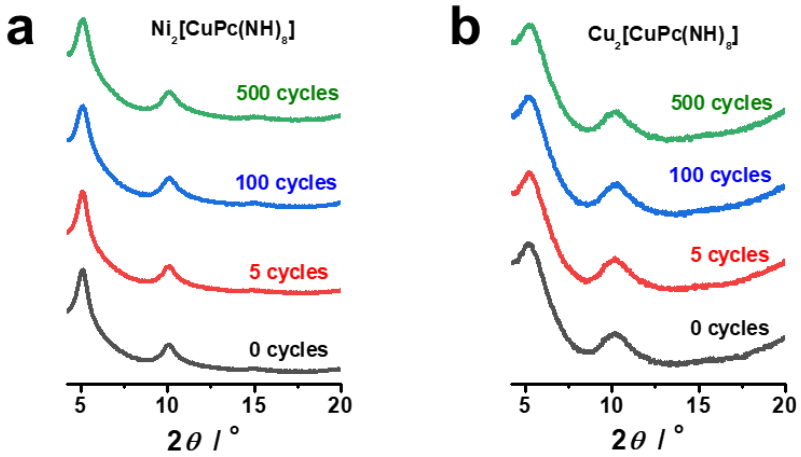

Figure S29. XRD patterns of (a) $Ni_2[CuPc(NH)_8]$ and (b) $Cu_2[CuPc(NH)_8]$ electrodes after different cycles at a current density of 10 A g^{-1}. The samples were measured with an X-ray diffractometer (Pananlytical Aeris Benchtop) in reflection geometry using Cu Kα radiation at room temperature.

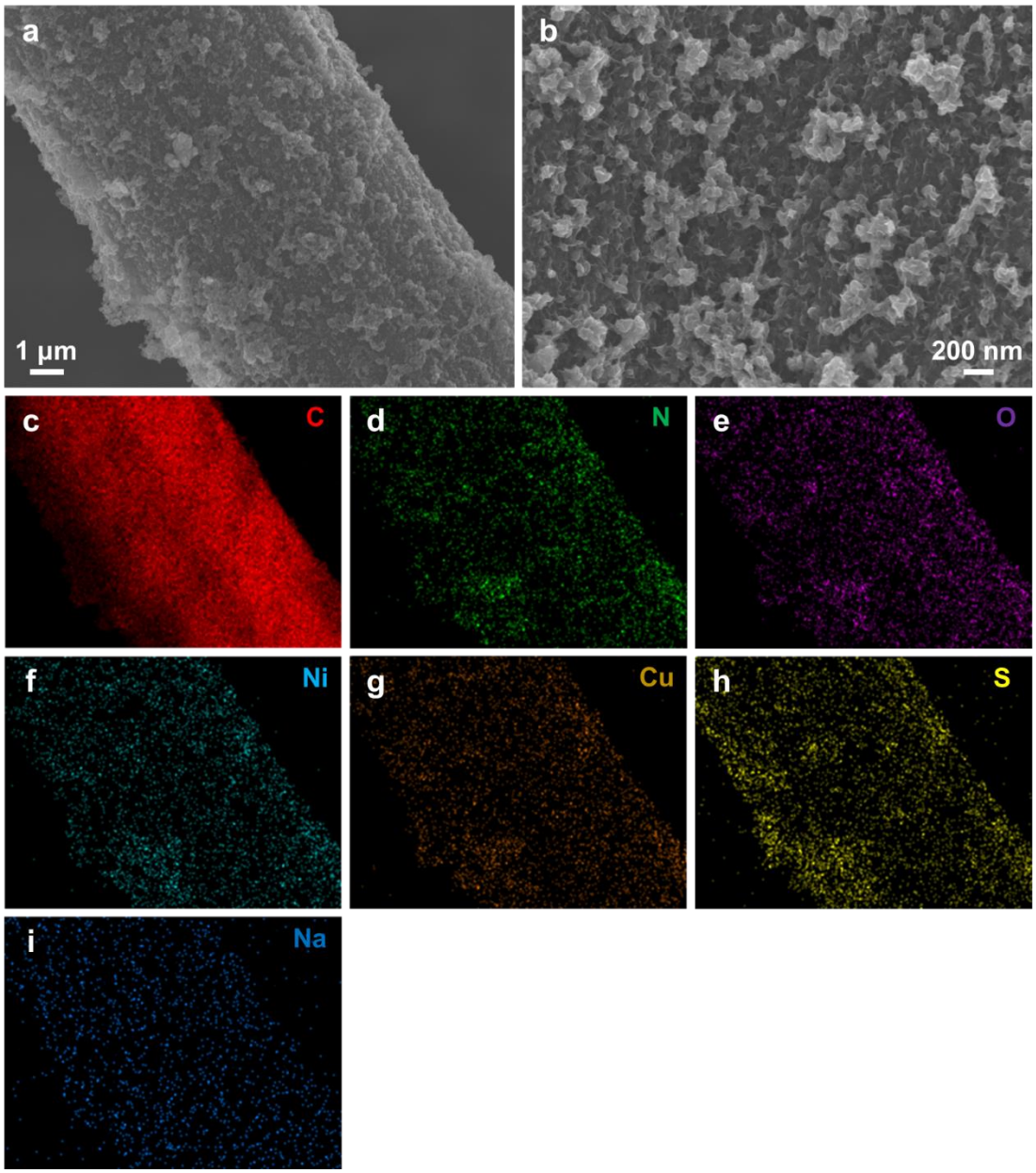

Figure S30. (a, b) SEM images of the $Ni_2[CuPc(NH)_8]$ electrode with different magnifications after 500 charge/discharge cycles. (c-i) Corresponding EDX elemental mapping analysis. The signals of O, S, and Na elements are from carbon cloth or adsorbed moisture/O_2 or electrolyte.

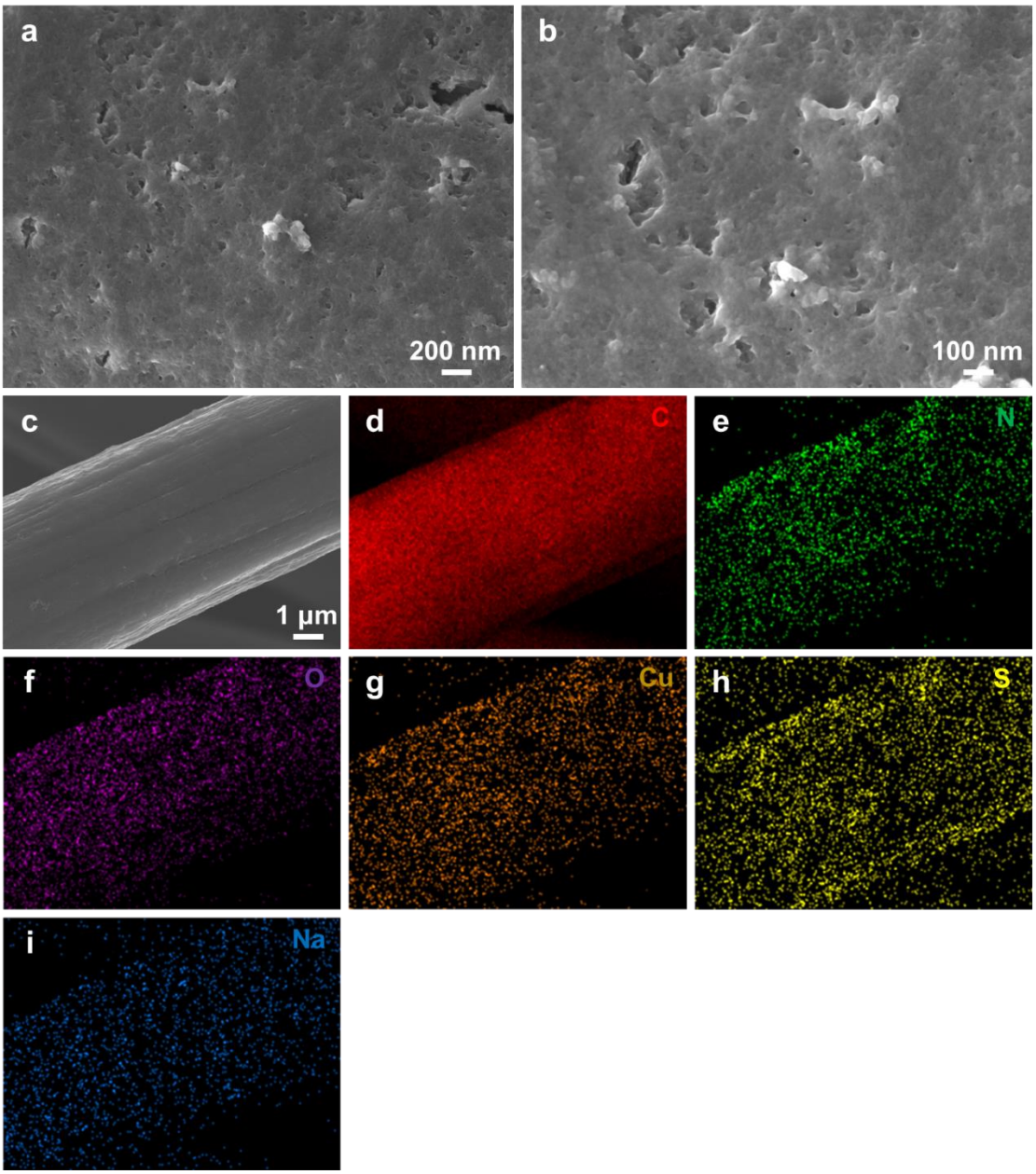

Figure S31. (a, b) SEM images of the $Cu_2[CuPc(NH)_8]$ electrode with different magnifications after 500 charge/discharge cycles. (c-i) Corresponding EDX elemental mapping analysis. The signals of O, S, and Na elements are from carbon cloth or adsorbed moisture/O_2 or electrolyte.

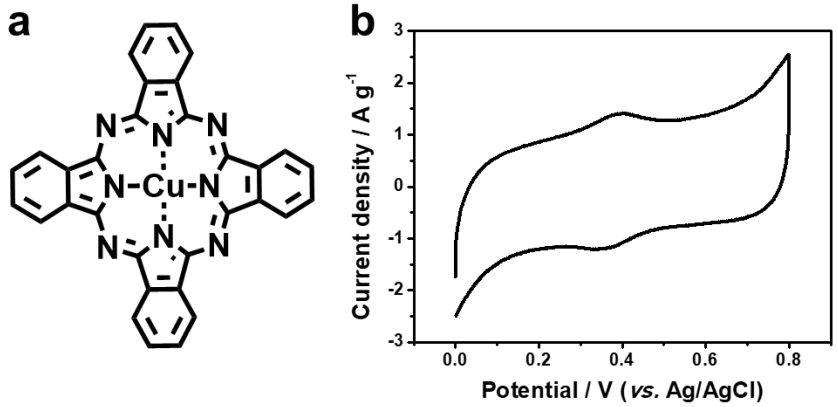

Figure S32. (a) Chemical structure of CuPc. (b) CV curve of CuPc at 10 mV s^{-1} in a three-electrode system.

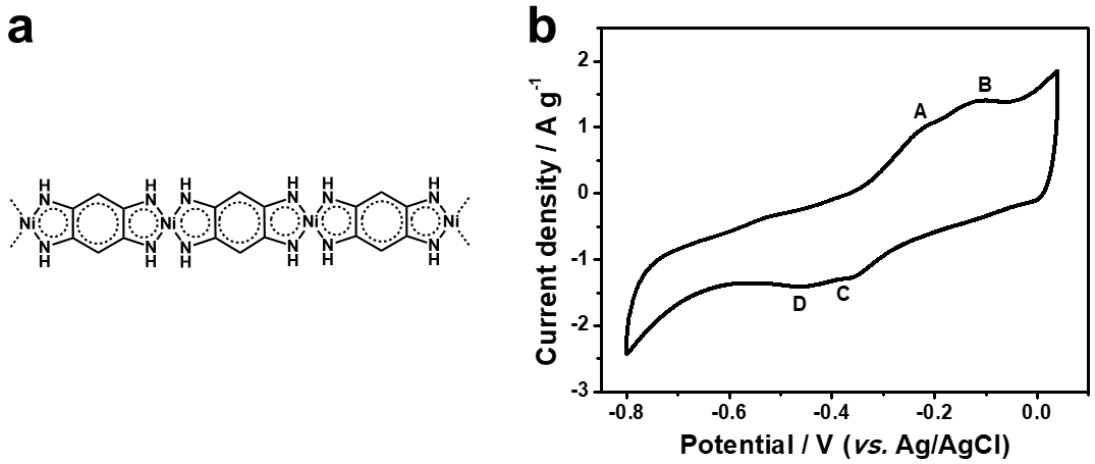

Figure S33. (a) Chemical structure of the Ni(BTI) coordination polymer. (b) CV curve of Ni(BTI) from 0.04 V (open-circuit potential) to −0.8 V at 10 mV s^{-1} in the three-electrode system.

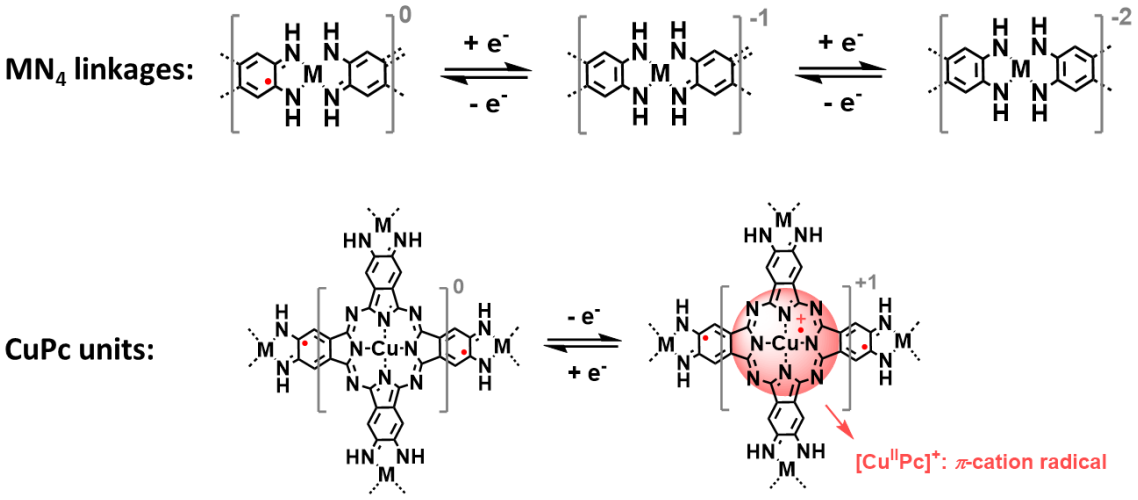

Figure S34. The electrochemical redox mechanism of MN_4 linkages and CuPc units in $M_2[CuPc(NH)_8]$.

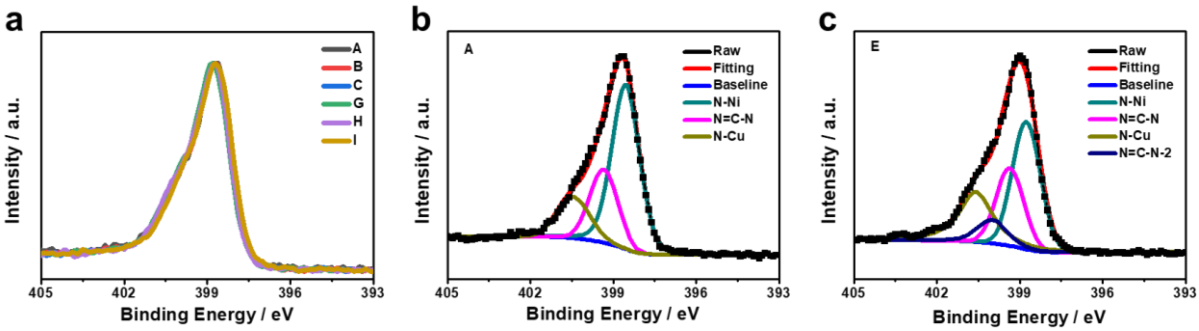

Figure S35. N *1s* XPS spectra of the $Ni_2[CuPc(NH)_8]$ electrode at different charge/discharge potentials.

As shown in Figure 3d and Figure S35a, negligible change in the N *1s* signal was detected for $Ni_2[CuPc(NH)_8]$ at potential of −0.8 V (@A and I in Figure S35a), −0.4 V (@B and H in Figure S35a), and 0 V (@C and G in Figure S35a). The N *1s* spectrum of $Ni_2[CuPc(NH)_8]$@A can be deconvoluted into three peaks at 400.4, 399.4, and 398.5 eV, corresponding to three types of N (N-Cu, N=C-N, and N-Ni, respectively) in the framework (Figure S35b). However, after the oxidation reaction of the phthalocyanine building block (0.8 V, @E), the N *1s* signal shifted by about +0.3 eV (Figure 3d and S35c). Deconvolution of the spectrum indicates the presence of an additional type of N, which is ascribed to the formation of π-cation radical in the phthalocyanine moiety.

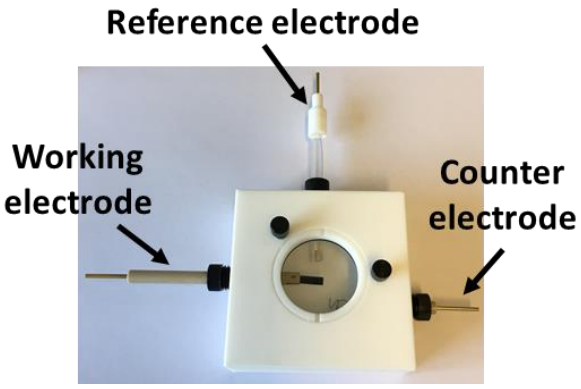

Figure S36. Digital photo of the three-electrode cell for *in-situ* Raman characterization.

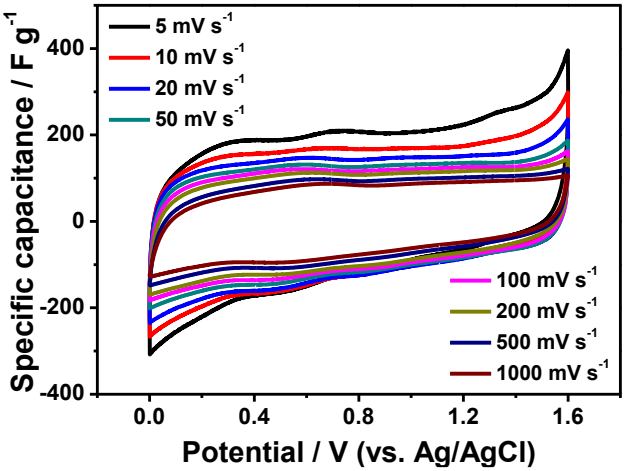

Figure S37. Normalized CV curves of $Ni_2[CuPc(NH)_8]$-SSCs from 5 to 1000 mV s^{-1}.

Table S1. Performance comparison of different electrode materials in liquid electrolyte (three-electrode system, at 0.5 A g^{-1}).

Materials	Electrolyte	Potential window (V)	Mass loading (mg cm^{-2})	Specific capacitance (F g^{-1})	Ref.
$Cu_3(HHTP)_2$	3 M KCl	0-0.5	0.6	202	[5]
$Cu_2[DBCO_8]$	1 M NaCl	-0.5-0.2	2.22	425	[6]
$Ni_3(HITP)_2$	3 M KCl	0-0.7	0.578	112	[7]
$Ni_3(HIB)_2$	1 M KOH	-0.75--0.25	8	410	[8]
$Ni_3(HITP)_2$	1 M $TEABF_4$/ACN	-0.6-0.5	5	83	[9]
PAN-*b*-PMMA-CFs	6 M KOH	0-0.8	1	360	[10]
Graphene	1 M H_2SO_4	0-1.0	1	198	[11]
Nanoporous MXene	3 M H_2SO_4	-0.5-0.3	11.2	351	[12]
Porous carbon	6 M KOH	0-1.0	-	280	[13]
rGO-aramid nanofibers	6 M KOH	0-1.0	1.5-2	122	[14]
Cr-doped δ-MnO_2	1 M Na_2SO_4	0-1.2	5	198	[15]
Graphene-activated carbon	6 M KOH	-1.0-0	-	345	[16]
Porous polymer	1 M Na_2SO_4	-1.2-0	-	250	[17]
N, P, O tri-doped carbon	6 M KOH	-1.15-0.1	-	348	[18]
Hierarchical porous carbon	1 M H_2SO_4	-0.2-0.9	1	240	[19]
$Ni_2[CuPc(NH)_8]$	1 M Na_2SO_4	-0.8-0.8	1.1	400	This work
$Ni_2[CuPc(NH)_8]$ thick electrode	1 M Na_2SO_4	-0.8-0.8	10	258.3	This work

Table S2. Performance comparison of typical symmetric SCs.

Electrodes	Electrolyte	Voltage window / V	Specific capacitance / F g^{-1}	Power density / W kg^{-1}	Energy density / Wh kg^{-1}	Cycling stability	Ref.
KNOSC	1 M Na_2SO_4	0-1.8	88.5 at 1 A g^{-1}	36000	39.8	20000 (90%)	[20]
Thionine–graphene	0.5 M Na_2SO_4	0-2.0	235 F $g_{electrode}^{-1}$ at 1 A g^{-1}	12000	32.6	10000 (91%)	[21]
NPCNs	PVA/H_2SO_4	0-1.0	58 at 1 A g^{-1}	24912.5	7.8	20000 (75%)	[22]
VN	PVA/LiCl	0-1.0	64 at 20 mV s^{-1}	3542	15.5	-	[23]
3D-PMCF	3 M H_2SO_4	0-1.0	74.1 at 5 mV s^{-1}	49900	23.9	10000 (86.3%)	[24]
MX-rHGO_3	3 M H_2SO_4	0-1.0	-	2400	11.5	10000 (93%)	[25]
TCNQ-CTF-800	$EMIMBF_4$	0-3.5	100 at 0.1 A g^{-1}	8750	42.8	5000 (92%)	[26]
h-CNS900	$BMIMBF_4$	0-3.0	165 at 0.1 A g^{-1}	2620	9.4	-	[27]
OCN	6 M KOH	0-1.0	-	5000	7	20000 (100%)	[28]
Cu_2[$DBCO_8$]	1 M NaCl	0-0.8	-	5000	13.8	2000 (80%)	[6]
ACWS-6	$EMIMBF_4$	0-4.0	216 at 0.5 A g^{-1}	25000	12	-	[13]
Cu_3(HHTP)$_2$	PVA/KCl	0-0.8	120 at 0.5 A g^{-1}	3000	3.3	5000 (85%)	[5]
c-CN	PVA/KOH	0.2-0.7	94 at 20 mV s^{-1}	2636	5.9	-	[29]
Ni_2[CuPc$(NH)_8$]	**Gelatin/Na_2SO_4**	**0-1.6**	**145 at 1 A g^{-1}**	**32084**	**51.6**	**5000 (90.3%)**	**This work**

References:

(1) Wang, M.; Ballabio, M.; Wang, M.; Lin, H. H.; Biswal, B. P.; Han, X.; Paasch, S.; Brunner, E.; Liu, P.; Chen, M.; Bonn, M.; Heine, T.; Zhou, S.; Canovas, E.; Dong, R.; Feng, X. Unveiling Electronic Properties in Metal-Phthalocyanine-Based Pyrazine-Linked Conjugated Two-Dimensional Covalent Organic Frameworks. *J. Am. Chem. Soc.* **2019,** *141*, 16810-16816.

(2) He, Y.; Yang, S.; Fu, Y.; Wang, F.; Ma, J.; Wang, G.; Chen, G.; Wang, M.; Dong, R.; Zhang, P.; Feng, X. Electronic Doping of Metal-Organic Frameworks for High-Performance Flexible Micro-Supercapacitors. *Small Struct.* **2021,** *2*, 2000095.

(3) Wang, Z. Y.; Wang, G.; Qi, H. Y.; Wang, M.; Wang, M. C.; Park, S.; Wang, H. P.; Yu, M. H.; Kaiser, U.; Fery, A.; Zhou, S. Q.; Dong, R. H.; Feng, X. L. Ultrathin two-dimensional conjugated metal-organic framework single-crystalline nanosheets enabled by surfactant-assisted synthesis. *Chem. Sci.* **2020,** *11*, 7665-7671.

(4) Park, J.; Hinckley, A. C.; Huang, Z.; Feng, D.; Yakovenko, A. A.; Lee, M.; Chen, S.; Zou, X.; Bao, Z. Synthetic Routes for a 2D Semiconductive Copper Hexahydroxybenzene Metal-Organic Framework. *J. Am. Chem. Soc.* **2018,** *140*, 14533-14537.

(5) Li, W. H.; Ding, K.; Tian, H. R.; Yao, M. S.; Nath, B.; Deng, W. H.; Wang, Y.; Xu, G. Conductive Metal-Organic Framework Nanowire Array Electrodes for High-Performance Solid-State Supercapacitors. *Adv. Funct. Mater.* **2017,** *27*, 1702067.

(6) Liu, J.; Zhou, Y.; Xie, Z.; Li, Y.; Liu, Y.; Sun, J.; Ma, Y.; Terasaki, O.; Chen, L. Conjugated Copper-Catecholate Framework Electrodes for Efficient Energy Storage. *Angew. Chem. Int. Ed.* **2020,** *59*, 1081-1086.

(7) Zhou, S.; Kong, X.; Zheng, B.; Huo, F.; Strømme, M.; Xu, C. Cellulose Nanofiber @ Conductive Metal-Organic Frameworks for High-Performance Flexible Supercapacitors. *ACS Nano* **2019,** *13*, 9578-9586.

(8) Feng, D.; Lei, T.; Lukatskaya, M. R.; Park, J.; Huang, Z.; Lee, M.; Shaw, L.; Chen, S.; Yakovenko, A. A.; Kulkarni, A.; Xiao, J.; Fredrickson, K.; Tok, J. B.; Zou, X.; Cui, Y.; Bao,

Z. Robust and conductive two-dimensional metal-organic frameworks with exceptionally high volumetric and areal capacitance. *Nat. Energy* **2018,** *3*, 30-36.

(9) Sheberla, D.; Bachman, J. C.; Elias, J. S.; Sun, C. J.; Shao-Horn, Y.; Dinca, M. Conductive MOF electrodes for stable supercapacitors with high areal capacitance. *Nat. Mater.* **2017,** *16*, 220-224.

(10) Zhou, Z.; Liu, T.; Khan, A. U.; Liu, G. Block copolymer-based porous carbon fibers. *Sci. Adv.* **2019,** *5*, eaau6852.

(11) Yang, X.; Cheng, C.; Wang, Y.; Qiu, L.; Li, D. Liquid-Mediated Dense Integration of Graphene Materials for Compact Capacitive Energy Storage. *Science* **2013,** *341*, 534-537.

(12) Fan, Z.; Wang, Y.; Xie, Z.; Xu, X.; Yuan, Y.; Cheng, Z.; Liu, Y. A nanoporous MXene film enables flexible supercapacitors with high energy storage. *Nanoscale* **2018,** *10*, 9642-9652.

(13) Shang, T. X.; Xu, Y.; Li, P.; Han, J. W.; Wu, Z. T.; Tao, Y.; Yang, Q. H. A bio-derived sheet-like porous carbon with thin-layer pore walls for ultrahigh-power supercapacitors. *Nano Energy* **2020,** *70*, 104531.

(14) Flouda, P.; Shah, S. A.; Lagoudas, D. C.; Green, M. J.; Lutkenhaus, J. L. Highly Multifunctional Dopamine-Functionalized Reduced Graphene Oxide Supercapacitors. *Matter* **2019,** *1*, 1532-1546.

(15) Zhao, Y.; Fang, Q.; Zhu, X.; Xue, L.; Ni, M.; Qiu, C.; Huang, H.; Sun, S.; Li, S.; Xia, H. Structure reinforced birnessite with an extended potential window for supercapacitors. *J. Mater. Chem. A* **2020,** *8*, 8969-8978.

(16) Huang, Y.; Shi, Y.; Gong, Q.; Weng, M.; Li, Y.; Gan, J.; Wang, D.; Shao, Y.; Zhao, M.; Zhuang, D.; Liang, J.; Pan, F.; Zhu, H.; Nan, C. Scalable preparation of hierarchical porous activated carbon/graphene composites for high-performance supercapacitors. *J. Mater. Chem. A* **2019,** *7*, 10058-10066.

(17) Peurifoy, S. R.; Russell, J. C.; Sisto, T. J.; Yang, Y.; Roy, X.; Nuckolls, C. Designing Three-Dimensional Architectures for High-Performance Electron Accepting Pseudocapacitors. *J. Am. Chem. Soc.* **2018,** *140,* 10960-10964.

(18) Cui, C.; Gao, Y.; Li, J.; Yang, C.; Liu, M.; Jin, H.; Xia, Z.; Dai, L.; Lei, Y.; Wang, J.; Wang, S. Origins of Boosted Charge Storage on Heteroatom-Doped Carbons. *Angew. Chem. Int. Ed.* **2020,** *59,* 7928-7933.

(19) Li, Q.; Dai, Z. W.; Wu, J. B.; Liu, W.; Di, T.; Jiang, R.; Zheng, X.; Wang, W. Z.; Ji, X. X.; Li, P.; Xu, Z. H.; Qu, X. P.; Xu, Z. M.; Zhou, J. Fabrication of Ordered Macro-Microporous Single-Crystalline MOF and Its Derivative Carbon Material for Supercapacitor. *Adv. Energy Mater.* **2020,** *10,* 1903750.

(20) Peng, H.; Yao, B.; Wei, X.; Liu, T.; Kou, T.; Xiao, P.; Zhang, Y.; Li, Y. Pore and Heteroatom Engineered Carbon Foams for Supercapacitors. *Adv. Energy Mater.* **2019,** *9,* 1803665.

(21) Shabangoli, Y.; Rahmanifar, M. S.; El-Kady, M. F.; Noori, A.; Mousavi, M. F.; Kaner, R. B. Thionine Functionalized 3D Graphene Aerogel: Combining Simplicity and Efficiency in Fabrication of a Metal-Free Redox Supercapacitor. *Adv. Energy Mater.* **2018,** *8,* 1802869.

(22) Kale, V. S.; Hwang, M.; Chang, H.; Kang, J.; Chae, S. I.; Jeon, Y.; Yang, J.; Kim, J.; Ko, Y. J.; Piao, Y. Z.; Hyeon, T. Microporosity-Controlled Synthesis of Heteroatom Codoped Carbon Nanocages by Wrap-Bake-Sublime Approach for Flexible All-Solid-State-Supercapacitors. *Adv. Funct. Mater.* **2018,** *28,* 1803786.

(23) Yi, Y. Y.; Yu, L. H.; Tian, Z. N.; Song, Y. Z.; Shao, Y. L.; Gao, L. J.; Sun, J. Y.; Liu, Z. F. Biotemplated Synthesis of Transition Metal Nitride Architectures for Flexible Printed Circuits and Wearable Energy Storages. *Adv. Funct. Mater.* **2018,** *28,* 1805510.

(24) Zhang, P.; Zhu, Q.; Soomro, R. A.; He, S.; Sun, N.; Qiao, N.; Xu, B. In Situ Ice Template Approach to Fabricate 3D Flexible MXene Film-Based Electrode for High Performance Supercapacitors. *Adv. Funct. Mater.* **2020,** *30,* 2000922.

(25) Fan, Z.; Wang, Y.; Xie, Z.; Wang, D.; Yuan, Y.; Kang, H.; Su, B.; Cheng, Z.; Liu, Y. Modified MXene/Holey Graphene Films for Advanced Supercapacitor Electrodes with Superior Energy Storage. *Adv. Sci.* **2018,** *5*, 1800750.

(26) Li, Y.; Zheng, S.; Liu, X.; Li, P.; Sun, L.; Yang, R.; Wang, S.; Wu, Z. S.; Bao, X.; Deng, W. Q. Conductive Microporous Covalent Triazine-Based Framework for High-Performance Electrochemical Capacitive Energy Storage. *Angew. Chem. Int. Ed.* **2018,** *57*, 7992-7996.

(27) Zhu, Q.-L.; Pachfule, P.; Strubel, P.; Li, Z.; Zou, R.; Liu, Z.; Kaskel, S.; Xu, Q. Fabrication of nitrogen and sulfur co-doped hollow cellular carbon nanocapsules as efficient electrode materials for energy storage. *Energy Storage Mater.* **2018,** *13*, 72-79.

(28) Liu, J.; Ji, L.; Wang, X.; Duan, L.; Zhou, J.; Jia, Y.; Zeng, S.; Huang, K.; Geng, Z.; Wang, X.; Hou, C.; Wu, X.; Lu, L.; Pei, Z.; Chen, Y.; Zhang, J.; Feng, S.; Zhang, Y. Commercial-Level Energy Storage via Free-Standing Stacking Electrodes. *Matter* **2019,** *1*, 1694-1709.

(29) Cai, J.; Song, Y.; Chen, X.; Sun, Z.; Yi, Y.; Sun, J.; Zhang, Q. MOF-derived conductive carbon nitrides for separator-modified Li-S batteries and flexible supercapacitors. *J. Mater. Chem. A* **2020,** *8*, 1757-1766.